Radio Frequency Front-End Filtering Circuit Based on Improved Coupled Microstrip Line Structure

Dan WANG, Qiaochu XIE

School of Network and Communication Engineering, Chengdu Technological University, Chengdu, 611730, China

QiaochuqcXie@outlook.com

Submitted March 13, 2026 / Accepted October 9, 2026 / Online first November 20, 2026

Abstract. *A multifunctional integration scheme based on improved coupled microstrip lines is proposed to address impedance mismatch, insertion loss, and volume redundancy in traditional discrete cascaded radio frequency front-ends. By embedding PIN diodes into a novel parallel coupled microstrip line configuration, a bias-controlled switching network is constructed, while a slow-wave resonant cavity and folded reference transmission line enable wideband filtering and dynamic phase adjustment. Prototype validation on a Rogers 4350B substrate demonstrates that the filter-switch module achieves ≤1.3 dB insertion loss over 0.55–0.75 GHz with ≥30 dB off-state isolation and 33.3% relative bandwidth. The filtering phase shifter attains ±0.9° phase accuracy within 2.5–4.1 GHz, delivers 27 W power capacity, and provides out-of-band suppression better than 55 dB/GHz. The proposed single-chip circuit integrates filtering, switching, and phase shifting, offering a compact solution for 5G transceivers and phased arrays.*

Keywords

Coupled microstrip line, radio frequency front-end, integrated circuit, filter switch, filter phase shifter

1. Introduction

In modern wireless communication systems, the radio frequency front-end (RFFE) serves as a critical interface connecting the digital baseband and the antenna, and is responsible for signal transmission and reception, as well as necessary signal processing, including amplification, filtering, and frequency conversion. Its performance directly affects the overall efficiency and quality of the entire communication system [1]. With the rapid advancement of Fifth Generation Mobile Communication (5G) technology, the requirements for RFFE have extended beyond simple signal amplification and filtering to encompass multi-band operation, wide bandwidth, high selectivity, and compact size. Although traditional discrete design methods, which involve designing filters, switches, and phase shifters (PSs) separately and combining them in a cascaded manner, can meet basic functional requirements, they often result in increased circuit complexity, higher losses, and higher costs, while also making it difficult to achieve the desired reduction in size [2], [3]. Consequently, research into how to integrate filtering, switching, and phase-shifting functions into a single chip through innovative design concepts and technical means has become the key to improving the performance of RFFEs. Current research in this area mainly focuses on multi-band implementation, broadband characteristic optimization, filtering and antenna integration, and low-noise reception. Although some progress has been made in these studies, the commonly used architecture is a separate cascaded structure of filters, switches, and PSs, which leads to impedance mismatch, increased insertion loss (IL), and increased volume [4]. As an important microwave transmission line structure, coupled microstrip lines (CMLs) play a crucial role in radio frequency circuit design. It achieves effective signal transmission and processing through the interaction of electromagnetic fields. CMLs not only have the advantages of easy integration, low cost, and stable performance, but also effectively reduce losses and parasitic effects, and improve system reliability [5]. To enhance the overall effectiveness of the RFFE circuit and integrate filtering, switching, and phase shifting functions on a single CML, research is conducted on improving the coupling structure, introducing a P-type intrinsic-N-type (PIN) diode bias network, and establishing a parity mode cooperative model to design low IL, high isolation filtering switches, and high-precision filtering PSs.

The innovation of this research lies in the development of a novel CML configuration that integrates a slow-wave resonant cavity and a folded reference transmission line within a single layout. This structure enables the simultaneous optimization of filtering selectivity, phase shift accuracy, and switching isolation—an achievement not realized in prior works using similar components. By introducing a PIN diode bias network to regulate the operating mode, and combining it with an even-odd mode collaborative model to analyze transmission zero points, impedance matching and frequency selectivity are optimized. Furthermore, a unique parallel-CML layout incorporating a compact slow-wave resonator and a folded reference line is proposed. This design not only saves space but also enables precise control of phase velocity matching and harmonic suppression, both of which are critical for wideband PS performance. The main contribution of this research lies in solving the impedance mismatch problem inherent in

DOI: 10.13164/re.2026.0631

traditional discrete cascade architectures, thereby achieving low IL, high isolation, and continuously reconfigurable phase control. This improves the integration and performance stability of RFFE circuits and provides technical support for the design of miniaturized and low-cost RFFEs.

The remainder of this paper is organized as follows. Section 2 reviews the related works. Section 3 presents the design and theoretical analysis of the filter switch and filtering PS based on improved CMLs. Section 4 provides the simulation and experimental results and discusses the performance of the proposed circuits. Finally, the main conclusions are summarized.

2. Related Works

The filtering and integration design of RFFE is the key to improving the performance of modern communication systems. Current research focuses on multi-band implementation, broadband characteristic optimization, filtering and antenna integration, and low-noise reception. P. Y. Qin et al. proposed a microstrip disk monopole antenna integrated with a reconfigurable bandpass filter. By embedding a three-line coupled resonator (TLCR) into the antenna feed structure and employing PIN diodes to switch the filter states, the antenna can dynamically toggle between wideband and narrowband operation—making it suitable for cognitive radio applications. Experimental results show that, in both operating modes, the antenna maintains consistent radiation patterns, low cross-polarization, and measured gains that align well with simulated values [6]. P. Rajian et al. used interconnected multi-mode resonators (MMRs) and multi-stage impedance structures to achieve a compact topology for multi-band bandpass filters, and utilized reverse biased varactor diodes to provide tuning capability. By changing a few geometric parameters of the MMR, fast and reliable synthesis of multi frequency response could be achieved. The results showed that the filter achieved four frequency bands at 1.8 GHz, 2.1 GHz, 2.7 GHz, and 3.4 GHz, with attenuation greater than –15 dB [7]. A. Kumar et al. designed a compact resonator loaded coupled line structure differential broadband bandpass filter and achieved good common mode harmonic suppression. They studied a four port design with a watch shaped configuration and divided the circuit into a dual port network along the symmetry plane to analyze the differential mode. By optimizing the length and width of the short section line, the filter was manufactured on a Rogers 5880 substrate for experimental verification. The results indicated that the proposed technology has achieved differential broadband bandpass characteristics through experimental verification [8]. E. Meyer et al. designed a new substrate integrated waveguide (SIW) base filter antenna for the 5G new radio sub-6 GHz communication. By using SIW base resonators and integrating radiating elements into the filter design, a third-order filtering response was generated using SIW base resonators and patch antenna elements. The results showed that the SIW pedestal filter antenna had a 10 dB return loss (RL) bandwidth of 4.29% and an axial gain of 3.66 dBi at the center frequency of 3.63 GHz [9]. S. Yun et al. designed a low-noise, high input second-order intermodulation point anti blocking receiver front-end for 5G new wireless cellular applications. They used dual radio frequency and baseband N-path filtering methods, reused the double balanced mixer in the main signal path to reduce the number of switches, and integrated components such as transformers and low-noise amplifiers. The results showed that the front-end noise figure of the receiver was 2.7 dB, the conversion gain was 43 dB, and the power consumption was 14.41 mW [10].

High selectivity filtering, precise phase modulation, and beamforming are the core technologies for RFFE adaptation to high-frequency communication and high-power applications. Related research focuses on coupling microstrip lines and modeling methods to improve the frequency selectivity, phase accuracy, and power capacity of circuits. F. Wei et al. presented a class of balanced filtering PSs. Using even-odd mode analysis, they modeled differential- and common-mode transmission characteristics separately, enabling independent control over phase response and common-mode suppression. By appropriately designing the electrical length and impedance ratio of coupled line sections, transmission zeros were introduced in the common-mode path, structurally enhancing common-mode rejection. Furthermore, by matching the phase variation rates between the filtered and reference paths, the differential-mode phase shift exhibits low frequency dependence across the passband [11]. H. Choi et al. designed a highly selective radio frequency filter using a novel quadruple structure that can generate a pair of transmission zeros. The structure consists of coupling lines with negative coupling characteristics and independent lines. The results indicated that the 2 GHz microstrip filter with a bandwidth of 7.5% could achieve precise design without coupling debugging [12]. J. Lee et al. adopted a frequency reconfigurable RFFE integrated circuit design method to achieve 28/37 GHz dual band beamforming in 5G communication. By integrating frequency reconfigurable variable gain PSs, dual band low-noise amplifiers, and high isolation switches, they achieved precise control of gain and phase. The results showed that the phase root mean square error of the circuit was less than 0.9°, the gain error was less than 0.23 dB, and the transmission efficiency was over 14% [13]. J. Cai et al. adopted a new PS design method based on the principle of adjustable electrical length to achieve phase control in high-power microwave systems. By rotating the choke piston in the annular phase shifting section to change the electrical length, continuous phase adjustment was achieved. The findings revealed that the PS exhibited a phase shift exceeding 360° within the 2.7–2.9 GHz frequency range, with a power capacity surpassing 450 MW. Additionally, it demonstrated a phase shift accuracy of 3.29°, a response time of 30 ms, an RL exceeding 12 dB, and an IL below 0.4 dB [14]. H. Li et al. applied radio frequency vector superimposed PSs to phased array front-end systems by using complex curve fitting and frequency/control voltage fitting for the PS orthogonal signal generator and variable gain amplifier, respectively. The

results indicated that the simulation results of the model were in good agreement with the measured data, verifying the effectiveness and usability of the model [15].

In summary, existing work has made progress in multi-band filtering, broadband common-mode suppression, integrated filtering antennas, and low-noise high-power front-ends. However, the widespread use of separate cascaded architectures of filters, switches, and PSs results in impedance mismatch, increased IL, and increased volume. Although filter PSs combine frequency selectivity and phase control, they inherently lack signal gating capability and require external switches to disconnect signal paths, which introduces additional IL and impedance discontinuities. Integrated filter-switch structures integrate filtering and switching functions but have no phase tuning ability, leaving separate PS modules indispensable in the system. Reconfigurable RF front-ends employ tunable components to support multi-band operation; nevertheless, their underlying topologies still adopt cascaded discrete functional modules, failing to address impedance mismatch and bulky size issues. The proposed design embeds PIN diode-controlled switching networks, slow-wave resonant filtering topologies, and folded reference transmission lines into a single modified CML configuration, outperforming the aforementioned discrete schemes. This monolithic integration eliminates inter-stage matching networks and reduces the overall footprint to 15 mm × 10 mm. Moreover, it achieves low IL, high isolation, and continuous phase control in a single circuit. Such a high level of integration has not been realized in existing filter PSs, filter switches, and reconfigurable front-end architectures.

3. Methodology

3.1. Filter Switch Integration Based on Coupled Microstrip Lines

Currently, RFFE systems often adopt a cascaded architecture of independently designed switches and filters, which can easily cause impedance mismatch problems, leading to increased circuit IL and degraded out of band suppression, resulting in increased manufacturing costs and design complexity of RFFE systems [16]. To this end, a single-chip integrated circuit based on CMLs and with dual functions of filtering and switching is proposed. The integrated circuit is shown schematically in Fig. 1.

As shown in Fig. 1, the access point is responsible for wireless access and signal forwarding of the device, while the modem is used for modulation, demodulation, and conversion of digital signals and radio frequency signals. The RFFE transceiver connects the wireless connection channel to various front-end components. This circuit integrates switches and filters in the RFFE, and achieves mode switching by regulating the bias voltage of external diodes. While improving system integration, it avoids impedance mismatch problems in traditional filter switch cascade architectures and reduces the manufacturing cost and design complexity of the circuit. Among them, CMLs have significant advantages such as easy integration, low cost, and stable performance, which can be directly integrated with other microwave components and facilitate miniaturization design. In addition, its electromagnetic coupling mechanism does not require additional connecting components, reducing losses and parasitic effects, and improving system reliability [17]. Therefore, the study uses CMLs to make microwave filter switches, and its structure and signal excitation are shown in Fig. 2.

In Fig. 2, under even mode excitation, the port voltage/current is in phase, while under odd mode excitation, it is in phase. The impedance representation of the four port network characteristics can be obtained by analyzing the physical relationship between voltage and current, as shown in (1) [18]:

$$Z_{\text{in}} = \sqrt{\frac{-\left(Z_{\text{oe}} + Z_{\text{oo}}\right)^2 \cos\delta^2 + \left(Z_{\text{oe}} - Z_{\text{oo}}\right)^2}{2\sin\delta}}. \tag{1}$$

In (1), Z_{in} is the input impedance, Z_{oo} and Z_{oe} are the odd mode impedance and even mode impedance, respectively, and δ is the electrical length. According to (1), when the electrical length δ approaches π or 0, the real part of the input impedance converges to zero, while the imaginary part exhibits a divergence characteristic of ±j∞. This impedance state reflects that the microstrip circuit is in the band impedance operating mode. When the real part of the impedance is non-zero, it corresponds to the passband transmission state. Based on this characteristic, a filtering circuit module composed of CMLs is studied and designed, as denoted in Fig. 3. Figure 3 presents (a) the coupling-line stub-loaded resonator, (b) the parallel-coupled feeding line, and (c) the equivalent schematic of the filtering circuit.

Figures 3(a) and 3(b) show the construction unit of the filter switch core. Study represents the voltage current transmission characteristics of a coupled line stub loaded resonator using the ABCD cascade matrix $\mathbf{H}_1$, as shown in (2):

$$\mathbf{H}_1 = \begin{bmatrix} A_1 & B_1 \\ C_1 & D_1 \end{bmatrix} = \begin{bmatrix} \dfrac{Z_{\text{oe1}} + Z_{\text{oo1}}}{Z_{\text{oe1}} - Z_{\text{oo1}}}\cos^2\delta_1 & \dfrac{\text{j}}{2}\dfrac{(Z_{\text{oe1}} + Z_{\text{oo1}})^2 \sin^2\delta_1}{Z_{\text{oe1}} - Z_{\text{oo1}}} - \dfrac{\text{j}2Z_{\text{oe1}}Z_{\text{oo1}}}{(Z_{\text{oe1}} - Z_{\text{oo1}})\sin\delta_1} \\ \dfrac{\text{j}2\sin\delta_1}{Z_{\text{oe1}} - Z_{\text{oo1}}} & \dfrac{Z_{\text{oe1}} + Z_{\text{oo1}}}{Z_{\text{oe1}} - Z_{\text{oo1}}}\cos^2\delta_1 \end{bmatrix}. \tag{2}$$

In (2), A_1, B_1, C_1, and D_1 are the four elements of the matrix, which respectively reflect the relationship coefficients between inputting and outputting currents, inputting voltage and outputting current, inputting current and outputting voltage, and inputting and outputting voltage [19]. Z_{oe1}, Z_{oo1}, and δ_1 respectively represent the odd mode, even mode characteristic impedance, and electrical length of the resonator. The ABCD cascade matrix $\mathbf{H}_2$ of parallel coupled feeding lines is denoted in (3).

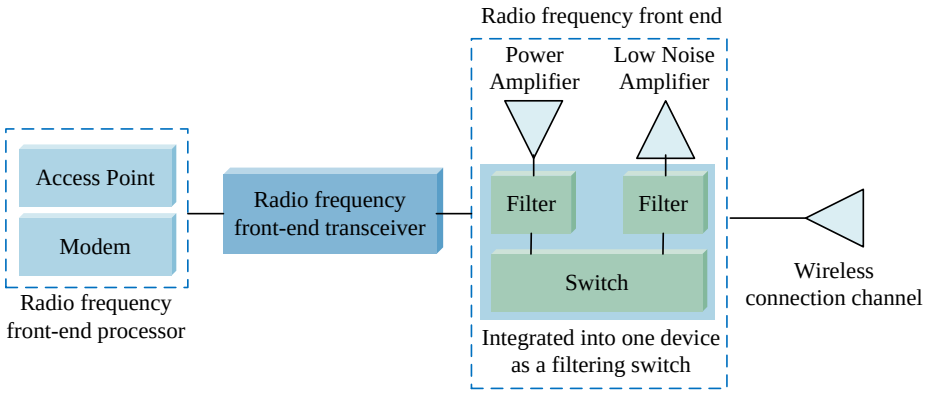


Fig 1. Schematic diagram of dual function filter-switching monolithic integrated circuit.

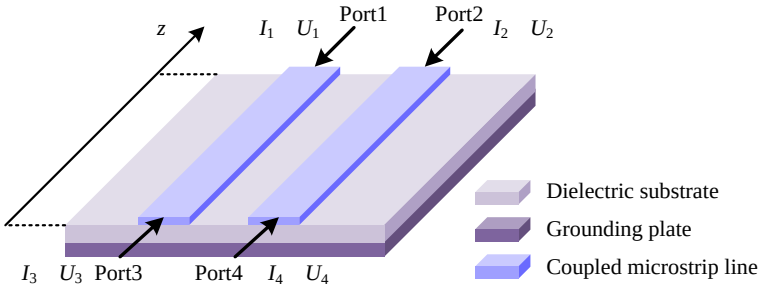
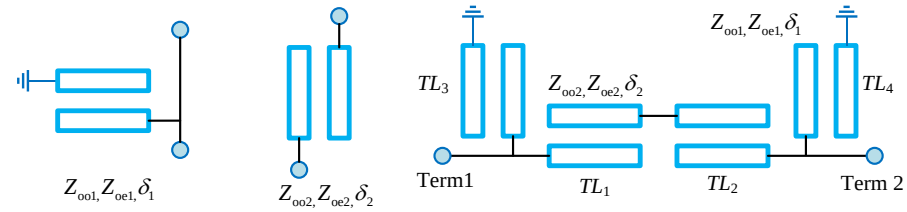


Fig. 2. Excitation diagram of coupled microstrip line signal.



(a) Stub loaded resonator coupled line (b) Parallel coupled feed line (c) Equivalent diagram of the filter circuit

Fig. 3. Filter circuit module.

$$\mathbf{H}_2 = \begin{bmatrix} A_2 & B_2 \\ C_2 & D_2 \end{bmatrix} = \begin{bmatrix} \dfrac{Z_{oe2}+Z_{oo2}}{Z_{oe2}-Z_{oo2}}\cos\delta_2 & \dfrac{\mathrm{j}(Z_{oe2}-Z_{oo2})^2-(Z_{oe2}+Z_{oo2})^2\cos^2\delta_2}{2(Z_{oe2}-Z_{oo2})\sin\delta_2} \\ \dfrac{2\mathrm{j}\sin\delta_2}{Z_{oe2}-Z_{oo2}} & \dfrac{Z_{oe2}+Z_{oo2}}{Z_{oe2}-Z_{oo2}}\cos\delta_2 \end{bmatrix}. \tag{3}$$

From (2) and (3), when the input impedance Z_{in1} is 0, the resonator will introduce a transmission zero (b_1,b_2) in the bandpass filter of the parallel coupling structure, as shown in (4):

$$\begin{cases} b_1 = \dfrac{2}{\pi}\arcsin\sqrt{1-\varepsilon_2^2}\, f_c < f_c \\ b_2 = 2f_c - b_1 > f_c \end{cases} \tag{4}$$

In (4), ε means the coupling coefficient of the resonator, and f_c means the center frequency at which the device operates. The generation of transmission zeros (TZ) originates from the combination of the odd-even mode synergy of CMLs and the bias regulation of PIN diodes. In the PCML structure, the characteristic impedances (Z_{oo}/Z_{oe}) and propagation constants of the odd and even modes have inherent differences. When signals are excited in different modes, energy cancellation effects are formed at specific frequencies. Specifically, the coupled line stub-loaded resonator (Fig. 3(a)) adjusts the odd-even mode impedance ratio (Z_{oo}/Z_{oe}) to induce a phase mutation of signals at specific frequencies within the resonator. When this phase mutation reaches 180°, the input and reflected signals cancel each other completely, forming a transmission zero. Meanwhile, the bias state of the PIN diode dynamically adjusts the equivalent impedance of the resonator: when forward-biased, the diode is equivalent to an LC series structure, which enhances the odd-even mode difference and shifts the transmission zero toward the target stopband; when reverse-biased, the diode is equivalent to an RL series structure, forming a low-impedance path that further strengthens the suppression of signals at specific frequencies, ultimately achieving high out-of-band isolation.

Figure 3(c) showcases the equivalent diagram of the filtering circuit, which is composed of two sets of CMLs. The middle part is a parallel coupled feeding line (TL1 and TL2), and the left and right sides are coupled line short section loaded resonators (TL3 and TL4).

For the switch module, after comprehensive evaluation of core elements such as switch device volume, high-frequency adaptability, and parameter measurability, the SMP1340-007LF PIN diode model is ultimately selected as the switch element. When an on-state bias is applied to the switch, its equivalent circuit can be modeled as an inductor capacitor series connection, exhibiting approximate open circuit characteristics in the high frequency range [20]. At this point, the integrated device activates the bandpass filtering function to achieve frequency selective transmission. Under the condition of off-state bias, the device is equivalent to a series connection of resistance and inductance, forming a low impedance path and exhibiting short-circuit characteristics [21], [22]. The ABCD matrix $\mathbf{H}_{FS}$ of the switch module and filter module is shown in (5).

$$\mathbf{H}_{FS} = \begin{bmatrix} A_{FS} & B_{FS} \\ C_{FS} & D_{FS} \end{bmatrix} = \begin{bmatrix} 1 & 0 \\ 1/Z_1 & 1 \end{bmatrix} \begin{bmatrix} A_2 & B_2 \\ C_2 & D_2 \end{bmatrix} \begin{bmatrix} D_2 & B_2 \\ C_2 & A_2 \end{bmatrix} \begin{bmatrix} 1 & 0 \\ 1/Z_1 & 1 \end{bmatrix}. \quad (5)$$

According to (5), the working index parameters of the entire module can be calculated, as shown in (6):

$$\begin{cases} \ell_R = \dfrac{A_{FS} + B_{FS}/Z_0 - C_{FS}Z_0 - D_{FS}}{A_{FS} + B_{FS}/Z_0 + C_{FS}Z_0 + D_{FS}} \\ \ell_I = \dfrac{2}{A_{FS} + B_{FS}/Z_0 + C_{FS}Z_0 + D_{FS}} \end{cases}. \quad (6)$$

In (6), ℓ_R and ℓ_I are the RL and IL of the filter switch, respectively, and Z_0 is the terminal impedance. The overall layout of the filter switch is shown in Fig. 4.

As shown in Fig. 4, the two module structures are jointly embedded in the main path of the microstrip line. When the PIN diode is connected to TL1 and the bias state is switched, the module can dynamically switch to the filtering function or the turn off suppression state, thus integrating the dual functions of filtering and switching in a single circuit.

3.2. Design of Filter Phase Shifter Based on Improved Coupled Microstrip Line

As the wireless communication technology develops, the requirements for RFFE circuits are increasing. They not only need to have efficient filtering functions, but also need to achieve precise control of signal phase. However, in traditional designs, filters and PSs often exist as independent units, and this separate architecture can easily lead to increased system complexity and performance degradation [23]. Therefore, research focuses on the collaborative implementation of filtering and phase shifting functions. By improving the parallel coupling structure and slow wave resonant cavity design, an optimization scheme for phase adjustment accuracy and filtering characteristics within a wide frequency band is constructed. For the main line filtering circuit of the PS, an improved microstrip line structure, namely parallel coupled microstrip line (PCML), is studied and designed. The equivalent circuit is denoted in Fig. 5. Figure 5 presents (a) the PCML structure, (b) the conventional parallel structure, and (c) the equivalent circuit of the PCML.

In Fig. 5(a), the PCML arranges Port 1 and Port 2 on the same side, forming a three wire coupling geometry. This structure has equivalent frequency domain response characteristics to the traditional cascaded structure in Fig. 5(b), and its bandpass filtering response (including transmission zero point distribution characteristics) can be modeled and analyzed through the traditional CML system matrix. When the electrical length is equal to one fourth of the guided wave wavelength, the structure exhibits a bandpass filtering response and generates enhanced TZ at the edge of the passband. In Fig. 5(c), the circuit contains two sets of anti PCMLs and dual terminal loading stubs. Due to

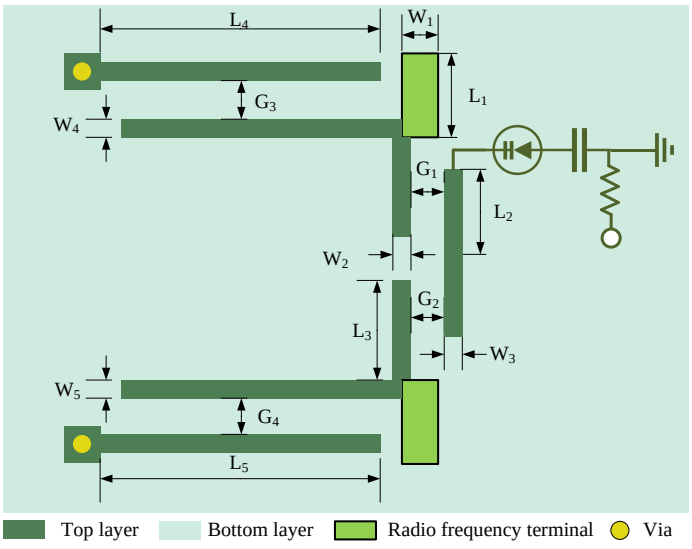
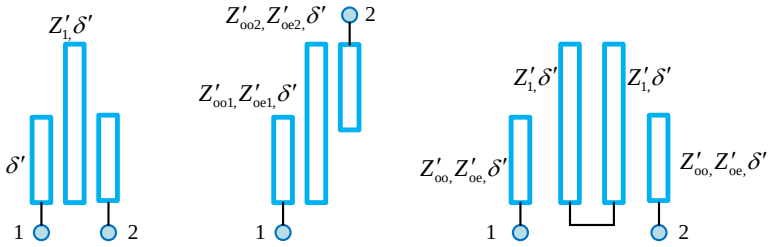
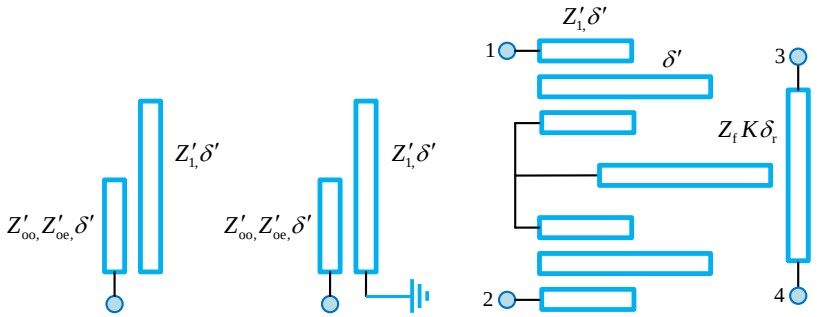


Fig. 4. Physical layout of filter switch.



(a) Coupled microstrip line structure (b) Traditional parallel structure (c) Equivalent circuit of coupled microstrip line

Fig. 5. Equivalent circuit of PCML.



(a) Coupled microstrip line structure (b) Traditional parallel structure (c) Microwave filter phase shifter circuit

Fig. 6. Equivalent circuit and main line filter circuit under different excitation modes.

the significant difference in electrical response of CMLs under symmetric and antisymmetric signal excitations, even mode and odd mode excitation states can respectively characterize the circuit characteristics under these two operating conditions. The study aims to convert the PCML structure into a simplified circuit under different excitation modes, providing a theoretical basis for analyzing the formation law of TZ. The equivalent circuit and main line filtering circuit under different excitation modes are denoted in Fig. 6. Figure 6 presents (a) and (b) the equivalent circuits under odd- and even-mode excitations, respectively, and (c) the microwave filter PS circuit.

Regarding Figs. 6(a) and 6(b), the study obtained the even mode input impedance Z'_{ie} of the PCML through odd even mode analysis, as shown in (7).

$$Z'_{ie}=\frac{\mathrm{j}(Z'_{oe}-Z'_{oo})^2}{(Z'_{oe}+Z'_{oo}+2Z'_1)\sin 2\delta'}-\frac{\cot\delta'(Z'_{oe}+Z'_{oo})\mathrm{j}}{2}. \quad (7)$$

In (7), Z'_{eo} is the even mode characteristic impedance of a PCML, which describes the impedance characteristics of the electromagnetic field when the currents of the two lines are in the same direction. It is determined by the width, spacing, and substrate parameters of the microstrip line. Z'_{oo} stands for odd mode impedance, which describes the impedance characteristics of the electromagnetic field when two wires have opposite currents and reflects the coupling strength. Z' is the characteristic impedance of the open circuit stub, attached to the impedance load at the coupling line port, used to regulate the transmission zero position [24]. The odd mode input impedance Z'_{io} is shown in (8):

$$Z'_{io}=-\frac{2\mathrm{j}\cot\delta Z'_{oe}Z'_{oo}}{Z'_{oe}+Z'_{oe}}. \quad (8)$$

In (8), Z'_{io} is used to determine the passband symmetry and center frequency. The TZ of the filter PS are generated by the synergy between the three-wire coupling geometry of the PCML and the load stubs. The three-wire structure of PCML (Fig. 5(a)) results in asymmetric electric field distribution between the odd and even modes, leading to differences in their phase velocities. When this difference accumulates to a specific value, signals form anti-phase superposition between the main transmission path and the coupling path, generating TZ. In addition, the terminal-loaded open stubs can precisely regulate the positions of TZ by adjusting their characteristic impedance: when the stub length is close to $\lambda_g/4$, an additional phase shift is introduced at the target stopband frequency, which superimposes with the odd-even mode phase difference of PCML to further enhance out-of-band suppression. Meanwhile, the mirror-symmetric layout of the dual CML units (Fig. 6(c)) can form symmetrical TZ on both sides of the passband, suppressing the second harmonic and spurious signals, thereby enhancing the frequency selectivity of the filter. According to the input impedance in different modes, the transmission zero position of the PCML can be further calculated, as shown in (9).

$$\begin{cases} b_d=\dfrac{2f'_c}{\pi}\arccos\sqrt{\dfrac{Z'_{oe}+Z'_{oo}}{Z'_{oe}+Z'_{oo}+2Z'_1}} \\ b_u=\pi-\dfrac{2f'_c}{\pi}\arccos\sqrt{\dfrac{Z'_{oe}+Z'_{oo}}{Z'_{oe}+Z'_{oo}+2Z'_1}} \end{cases}. \quad (9)$$

In (9), b_d and b_u are the lower sideband TZ and upper sideband TZ, respectively, and f_c' is the frequency corresponding to the electrical length δ' being $\pi/2$. As shown in Fig. 6(c), to balance passband characteristics and structural compactness, the main line filter adopts a double CML unit mirror symmetric layout. In addition, to suppress the second harmonic distortion caused by odd-even mode phase velocity mismatch, compensation open circuit stubs are introduced at key nodes of the filtering network [25]. On the basis of the main line filter, a reference transmission path consisting of characteristic impedance Z_f and electrical length $K\delta_r$ is added. The phase offset $\Delta\phi$ of the device is defined as the phase difference between the signal transmitted through the main line and the reference path, as shown in (10).

$$\Delta\phi = \phi_m - \phi_r. \tag{10}$$

In (10), ϕ_m and ϕ_r denote the insertion phase shifts of the main line and reference line, respectively. The values of ϕ_m and ϕ_r are shown in (11).

$$\begin{cases} \phi_m = \angle \ell_R \\ \phi_r = \angle \ell_I = -K\delta_r \end{cases}. \tag{11}$$

In (11), $\angle\ell_R$ and $\angle\ell_I$ are the phase angles of RL and IL, K is a real constant, δ_r denotes the electrical length of the reference transmission line, and $-K\delta_r$ represents the phase change of the reference line. In actual working conditions, to make the passband range of the main line filter consistent with the phase shift, it is necessary to make the reference line and the main line have the same phase change rate, as denoted in (12):

$$\left.\frac{d\phi_m}{d\delta}\right|_{f=f_c} = \left.\frac{d\phi_r}{d\delta}\right|_{f=f_c} = -\frac{\delta_c K}{f_c}. \tag{12}$$

In (12), δ_c is the electrical length at the center frequency. The Advanced Design System simulation software is utilized to analyze and calculate the physical parameters of a printed circuit board with copper deposition of 40 μm and a dielectric substrate model of Rogers 4350B. Due to the need for PSs to achieve a large phase offset, spatial folding topology reconstruction of the reference line is required to meet the coplanarity constraint between the reference path and the main filter terminal port. The physical layout of the PS is denoted in Fig. 7.

Figure 7 showcases the physical layout of the microwave filter PS, which is based on the equivalent circuit of Fig. 6. On the right side of the layout is the reference line structure, and on the left side is the main line filter. The physical schematic diagram of the filter switch and phase shifter in the research design is shown in Fig. 8.

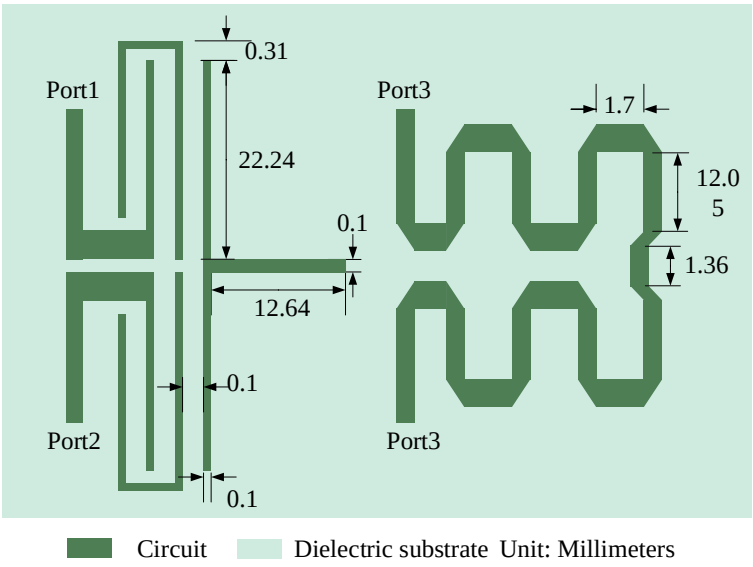
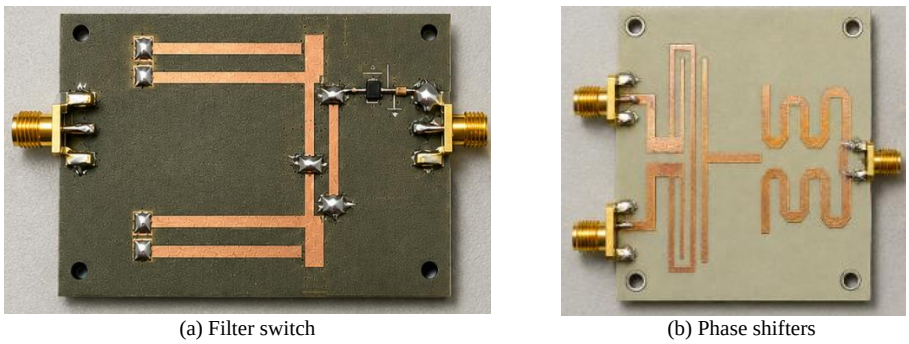


Fig. 7. Physical layout of phase shifters.



(a) Filter switch (b) Phase shifters

Fig. 8. Physical schematic diagram of the filter switch and phase shifter.

4. Results and Analyses

4.1. Testing of Filter Switches Based on Improved Coupled Microstrip Lines

To verify the actual performance of the integrated design of filter switches based on improved CMLs, a physical prototype was tested and analyzed. The IL, RL, and turn off suppression capability of the focusing filter switch in both on and off states were tested. By comparing simulation and actual measurement results, the effect of the CML structure and PIN diode collaborative design was verified, and the performance of the improved architecture in impedance matching, out of band suppression, and integrated function implementation was evaluated. Based on the excitation effect of external equivalent switch devices (optimized by Advanced Design System software), and after adjusting the physical dimensions of the prototype, the physical dimensions of the filter switch were finally obtained. Among them, W1–W5 in Fig. 4 were 2.41 mm, 0.28 mm, 0.32 mm, 0.35 mm, and 0.42 mm, respectively; L1–L5 were 18.22 mm, 75.50 mm, 70.04 mm, 73.87 mm, and 72.66 mm, respectively; G1–G5 were 0.20 mm, 0.18 mm, 0.19 mm, and 0.15 mm respectively. The dielectric substrate model of the filter switch used in the experiment was Rogers 4350B, with a center frequency of 0.6 GHz. The remaining experimental tests are denoted in Tab. 1.

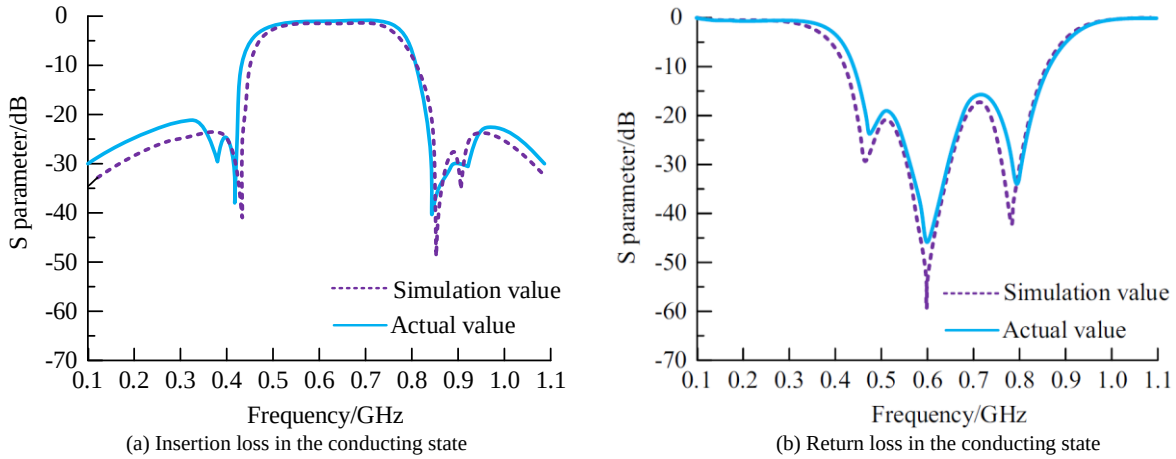
The proposed multifunctional integrated scheme comprises two core modules fabricated on a single Rogers 4350B substrate, forming a key part of a reconfigurable RF front-end system: The filtering switch module, operating in the 0.55–0.75 GHz band, performed signal gating and initial frequency selection. The filtering PS, operating in the 2.5–4.1 GHz band, provided simultaneous filtering and precise phase control for high-frequency signals. The two modules were interconnected via microstrip-line interfaces on the same substrate and could be dynamically activated or switched according to the communication system's frequency-band requirements, together delivering an integrated front-end solution spanning from mid-low to mid-high frequencies.

To receive radio frequency signals, Murata capacitors (470 pF) were soldered onto the radio frequency substrate. When applying a steady-state DC bias voltage, the polarity of the bias voltage was switched to regulate the conduction/cutoff state of the external diode, achieving the switching of the working mode of the filter switch prototype. Finally, the response curves of the RL and IL parameters under conduction and turn off states were measured. The measured and simulated values of the filter switch loss in the conducting state are denoted in Fig. 9. Figure 9(a) showcases the S-parameter curve of the IL of the filter switch, and Figure 9(b) showcases the S-parameter curve of the RL of the filter switch. Here, "Actual value" refers to the measured data from the prototype obtained using a vector network analyzer, while "Simulated value" represents the predicted value from an Advanced Design System simulation.

According to Fig. 9(a), the measured IL of the filter switch in the conducting state was consistent with the overall trend of the simulation values. The S-parameter of IL at the testing center frequency of 0.6 GHz was 1.3 dB, which was basically consistent with the simulation value, indicating good impedance matching of the port and weak

Parameter Name	Parameter Value
Center Frequency	0.6 GHz
Dielectric Substrate (Rogers 4350B)	Dielectric constant 3.48, thickness 0.508 mm, loss tangent 0.0037
PIN Diode (SMP1340-007LF)	Equivalent inductance 0.6 nH, equivalent resistance 0.13 Ω; equivalent capacitance 2 pF
Microstrip Line Odd and Even Mode Impedances	Z_{oe1} = 195 Ω, Z_{oo1} = 86.4 Ω, Z_{oe2} = 176.8 Ω, Z_{oo2} = 69 Ω
External DC Voltage	16 V
Termination Impedance	50 Ω

Tab. 1. Experimental parameters.



(a) Insertion loss in the conducting state

(b) Return loss in the conducting state

Fig. 9. The measured and simulated curves of insertion loss and return loss of filter switches.

signal reflection. –3 dB bandwidth covered 0.55–0.75 GHz. The out of band suppression was better than 20 dB, which verified the effective introduction of TZ by the CML resonator. In Fig. 9(b), the measured S-parameter of the passband RL was better than 15 dB, while the simulated value was slightly lower. The difference is mainly due to the small impedance shift caused by etching errors in the PIN diode packaging pads and microstrip lines. Overall, the performance of the prototype was consistent with the simulation trend. The improved coupling structure achieved a low IL of 1.3 dB at the center frequency, which was an improvement compared to typical discrete filter-switch cascades that often exhibit IL above 2.0 dB. This reduction in loss is primarily attributed to the elimination of inter-stage impedance matching networks and the minimized parasitic effects through monolithic integration. The measured and simulated values of the filter switch loss in the off state are denoted in Fig. 10. Figure 10(a) showcases the S-parameter curve of the IL of the filter switch, and Figure 10(b) showcases the S-parameter curve of the RL of the filter switch.

According to Fig. 10(a), the measured isolation (i.e., magnitude of the transmission coefficient) in the off state was below –30 dB over the range of 0.42 GHz to 0.94 GHz, showing a small deviation from the simulated value. This indicates that under reverse bias, the PIN diode exhibits a high-impedance state dominated by its junction capacitance. This, in conjunction with the stop-band rejection of the coupled microstrip and resonant structures, gives rise to the observed signal isolation. The result verifies that the high-impedance behavior of the diode under reverse bias, combined with the filtering structure, effectively blocks the signal path and achieves excellent isolation performance. The small fluctuations in the low-frequency range were caused by the parasitic inductance of the test fixture, but had almost no effect on the overall suppression. According to Fig. 10(b), the measured results of the turn off state RL were higher than 6 dB in the frequency range of 0.42 GHz–0.94 GHz, and the simulation values were slightly better. The difference is mainly introduced by the edge capacitance between the solder pad and the microstrip transition section. Most of the reflected energy at the port was absorbed by the load, further reducing the leakage power. Overall, the test results of high isolation and low reflection in the off state verify the effectiveness of the improved coupled microstrip structure and PIN diode co-design, providing reliable off suppression capability for the RFFE. The measured low IL and high isolation were explained by the field-circuit co-design strategy. In the ON state, monolithic integration eliminated bond wire transitions and inter-stage matching networks, which typically introduce 0.5–1.0 dB extra loss in cascaded filter-switch chains. Current flowed smoothly through low-loss copper microstrips with minimal reflection discontinuities. In the OFF state, the 2 pF capacitance of reverse-biased PIN diodes resonated with inductance of coupled-line stubs to form a parallel LC circuit. Its impedance peak coincided with the transmission zero generated by even- and odd-mode phase cancellation. At this frequency, electromagnetic energy was confined in resonators and reflected

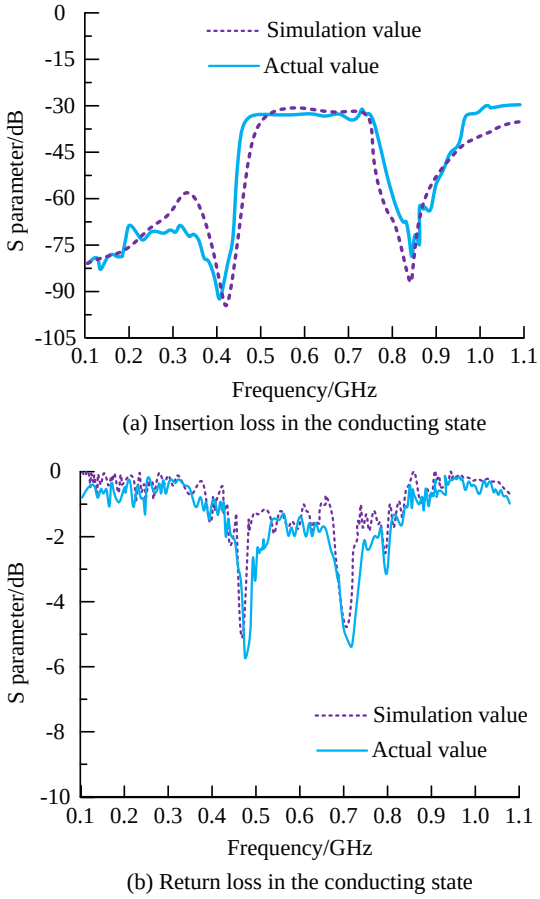


Fig. 10. Measured and simulated values of filter switch loss in the off state.

in-phase to the input, yielding 30 dB isolation at the output. This resonance-enhanced isolation was superior to the impedance blocking of discrete switches, since distributed resonators reflect unwanted energy instead of dissipating it into heat. To further verify the performance advantages of improving the CML structure, the designed filter switch was compared with existing related research filter switches. The performance comparison of filters from different studies is denoted in Tab. 2.

According to Tab. 2, the improved CML structure proposed in the study had certain advantages in the field of RFFE integration, with an IL of only 1.30 dB, which was superior to adjustable filters [26] (2.33 dB) and millimeter wave switches [27] (3.48 dB), and close to filter antennas [9] (0.92 dB). However, the filter switches designed in the study had higher integration. The turn off suppression reached 30.0 dB, which was an improvement of $\geq$ 1.9 dB compared to existing switch filter designs [26] (25.3 dB) and [27] (28.1 dB). The relative bandwidth was 33.3%, which was close to the broadband filter [8] (39.7%), and significantly wider than narrowband designs [7] (7.3%) and reference [9] (4.31%).

4.2. Testing of Filter Phase Shifter Based on Improved Coupled Microstrip Line

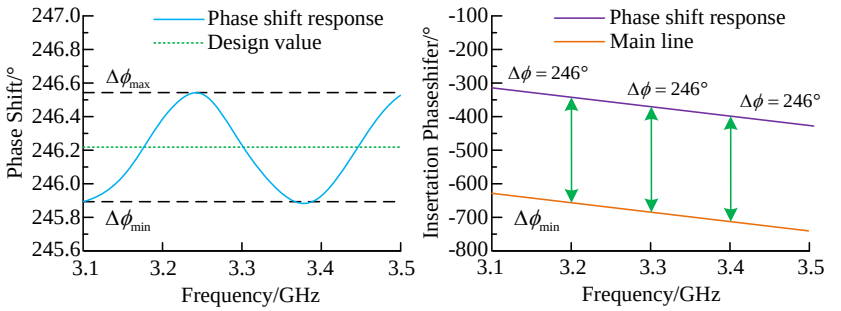
To verify the performance of the filter PS design based on improved CMLs, Advanced Design System soft-

ware was applied for electromagnetic simulation to extract the phase shift characteristics and their rate of change of the microwave filter PS. The simulation analysis results are shown in Fig. 11.

In Fig. 11(a), within the passband range of 3.1 GHz–3.5 GHz, the phase shift value of the PS remained stable at around 246°, and the phase deviation between the main line and the reference line of the PS was less than 0.4°, with small phase shift fluctuations. This indicated that the improved PCML structure was effective in compensating for the phase velocities of various modes. In Fig. 11(b), within the operating frequency band, the phase shift difference remained stable at 246°, and there was no significant fluctuation in the insertion phase slope, indicating that

Physical prototype comparison	Center frequency (GHz)	Passband (GHz)	Return loss (dB)	Insertion loss (dB)	Shutdown inhibition (dB)	Relative bandwidth (%)	Size (mm × mm)	Function integration
Reference [7]	Multi-band	1.8 / 2.1 / 2.7 / 3.4	15.2	2.83	/	7.3	20 × 15	Multi-frequency filtering
Reference [8]	2.5	~2.0–3.0	22.3	1.78	/	39.7	25 × 20	Broadband filtering + common mode suppression
Reference [9]	3.63	~3.55–3.71	10.1	0.92	/	4.31	30 × 25	Integrated filter antenna
Reference [26]	2.4	~2.22–2.58	18.7	2.33	25.3	15.2	18 × 12	Adjustable filter
Reference [26]	28	~25.4–30.6	14.5	3.48	28.1	18.3	12 × 8	Switch + filter
Reference [28]	27	24–30	11.9	5.17	/	22.2	22 × 18	Phase shift + filter
This study	0.6	0.55–0.75	15	1.3	30	33.3	15 × 10	Filter + switch + phase shift single chip integration

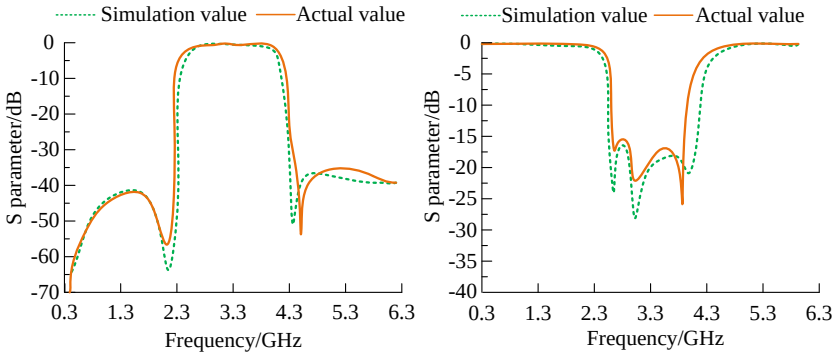
Tab. 2. Comparison of filter performance in different studies.



(a) Phase shift curve between the reference line and the main line of the phase shifter

(b) Phase slope of the phase shifter at 246°

Fig. 11. Phase shift characteristics and rate of change of microwave filter PS.



(a) Insertion loss in the conducting state

(b) Return loss in the conducting state

Fig. 12. S-parameter curve of insertion loss and return loss of physical prototype.

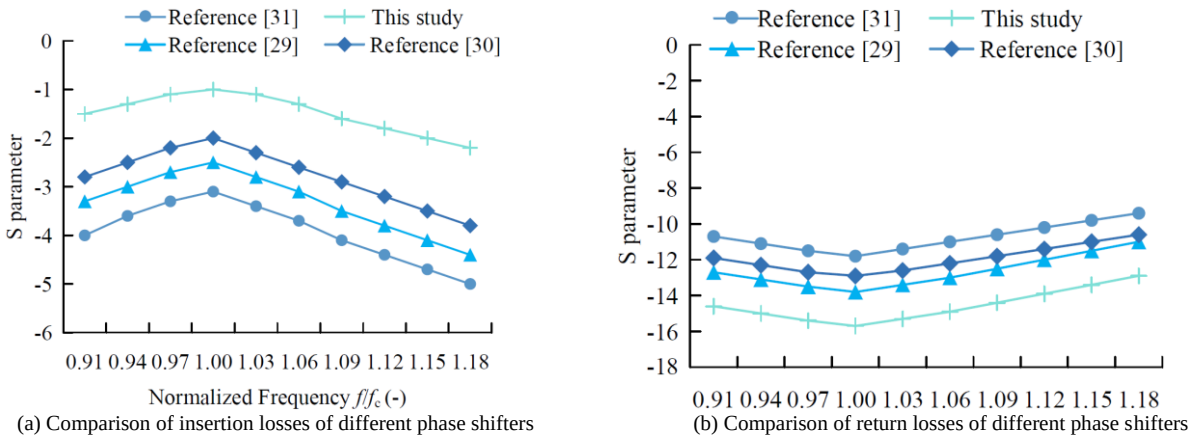
the PS had good performance consistency at the target phase shift value. The pre-simulation results verified the effectiveness of the filtering PS and met the prototype processing and testing standards. Based on the above key parameter analysis, the Rohde&Schwarz ZNB vector network analyzer was further utilized to test the PS and filtering functions of the prototype. The filtering function test results are denoted in Fig. 12. Figure 12(a) shows the S-parameter curve of IL for the physical prototype, and Figure 12(b) showcases the S-parameter curve of RL.

According to Fig. 12(a), the measured curve showed an IL of less than 1 dB in the 2.5 GHz–4.1 GHz passband, and an IL of only 0.65 dB at the center frequency (3.0 GHz), which was almost identical to the simulation value. At 2.1 GHz and 4.4 GHz, due to the introduction of TZ, the measured suppression was 57 dB and 55 dB, respectively. In Fig. 12(b), the measured RL within the passband was better than 15 dB. At the center frequency, the measured loss was only 0.7 dB higher than the simulated value (18.6 dB). Edge fluctuations were caused by pad parasitism, but the overall matching was good. The consistent trend of the two curves validated the effectiveness of the improved coupling structure in terms of IL, selectivity, and matching design. Broadband low-loss filtering and precise phase control were realized via targeted field manipulation in the modified PCML topology. The three-line coupled structure redistributed electric fields toward the substrate center, balancing even/odd-mode phase velocities and suppressing modal dispersion that degrades phase performance in traditional two-line couplers. Consequently, the phase response of the main filtering path closely matched that of folded reference lines across 2.5–4.1 GHz, with phase error maintained within ±0.9°. Regarding power handling, slow-wave resonators concentrate the longitudinal electric field within the low-loss dielectric region, reducing the peak surface current density by approximately 30% compared with conventional straight resonators of the same electrical length. Folded reference lines expanded the effective heat dissipation area without increasing circuit size. Benefiting from the above field shaping effects, the circuit supported a power rating of 27 W. In comparison, conventional microstrip PSs failed at just half this value due to concentrated edge current and severe ohmic loss. To conduct a more comprehensive evaluation of the proposed multi-functional circuit, further comparisons were made between the filter PS module and designs inherently integrating filtering and phase-shifting functions, as shown in Tab. 3.

In Tab. 3, the proposed circuit achieved the lowest IL (0.65 dB), minimum phase error (±0.9°), and the highest power density (27.0 W) compared to conventional filter PSs, while uniquely integrating a PIN diode-controlled switching network within the same improved coupled microstrip layout. To assess the superiority of the filter PS based on improved CMLs compared to other methods, the latest relevant research (references [29], [30], and [31]) was compared and tested. With normalized frequency as the x-axis, the effect of center frequency differences was eliminated. The loss comparison of different PSs is denoted in Fig. 13. Figures 13(a) and 13(b) show the comparison of IL and RL for different PSs, respectively.

Ref.	Center Freq. (GHz)	Passband (GHz)	Insertion Loss (dB)	Return Loss (dB)	Phase Error (°)	Power Handling (W)	Functional Integration
[11]	2.0	1.6–2.4	1.8	14.0	2.0	15.0	Filtering + Phase Shifting
[29]	3.5	2.5–4.5	2.5	13.8	2.5	17.5	Filtering + Phase Shifting
[30]	3.0	2.4–3.6	2.0	12.9	2.1	20.0	Filtering + Phase Shifting
[31]	31.25	24.0–38.5	3.1	11.8	3.2	13.5	Continuously Tunable Phase Shifting
[32]	2.4	1.9–2.9	2.2	12.5	3.5	12.0	Filtering + 90° Phase Shifting
[33]	2.0	1.5–2.5	2.8	12.5	3.2	16.0	Reconfigurable Filtering + Phase Shifting
This study	3.0	2.5–4.1	0.65	15.0	0.9	27.0	Filtering + Phase Shifting + Switching

Tab. 3. Performance comparison of filtering PSs with intrinsic bandpass response.



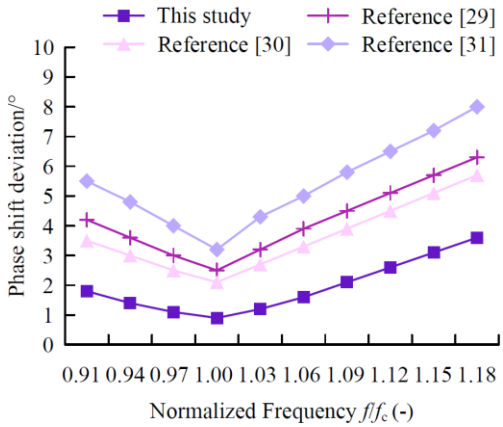
(a) Comparison of insertion losses of different phase shifters

(b) Comparison of return losses of different phase shifters

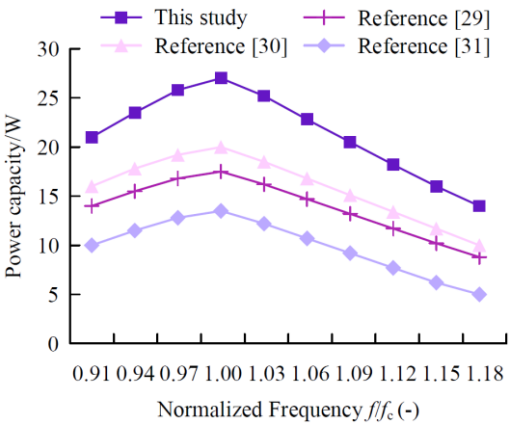
Fig. 13. Comparison of loss of different phase shifters.

From Fig. 13(a), within the normalized frequency range, the IL performance of the PS designed in this study was superior to the comparative study. At the center frequency (normalized frequency = 1.00), the IL was as low as 1.0 dB, which was 1.5 dB, 1.0 dB, and 2.1 dB lower than those in references [29] (2.5 dB), [30] (2.0 dB), and [31] (3.1 dB), respectively. As the frequency deviated from the center value, the IL of the designed PS increased more slowly. When the frequency increased from 1.00 GHz to 1.18 GHz, the loss only increased by 1.2 dB, while references [29], [30], and [31] increased by 1.9 dB, 1.8 dB, and 1.9 dB, respectively, indicating that it had better stability in maintaining low IL over a wide frequency range. From Fig. 13(b), at the center frequency, the absolute value of the RL of the designed PS reached 15.7 dB, which was higher than that of references [29] (13.8 dB), [30] (12.9 dB), and [31] (11.8 dB), indicating better impedance matching and less signal reflection, verifying the effectiveness of the improved coupling structure in improving matching stability. The phase adjustment accuracy and power carrying capacity of different PSs are denoted in Fig. 14. Figures 14(a) and 14(b) show the comparison of phase shift deviation (PSD) and power capacity of different PSs, respectively.

According to Fig. 14(a), the improved CML PS had lower PSD across all frequency bands compared to the comparative literature. At the center frequency, the PS deviation



(a) Comparison of phase shift deviations of different phase shifters



(b) Comparison of power capacity of different phase shifters

Fig. 14. Phase adjustment accuracy and power carrying capacity of different phase shifters.

of the PS was only 0.9°, which was 64%, 57%, and 72% lower than reference [29] (2.5°), reference [30] (2.1°), and reference [31] (3.2°), respectively, demonstrating high phase accuracy. As the frequency deviated, the deviation of the PS designed in the study increased more slowly, with only a 2.7° increase from 1.00 GHz to 1.18 GHz, while references [29], [30], and [31] increased by 3.8°, 3.6°, and 4.8°, respectively, to verify the wideband stability of their phase modulation. As shown in Fig. 14(b), the power capacity advantage of the PS designed in the study was significant, reaching 27.0 W at the center frequency, which was 54%, 35%, and 100% higher than reference [29] (17.5 W), reference [30] (20.0 W), and reference [31] (13.5 W), respectively, indicating a stronger carrying capacity. When the frequency deviated, the PS designed for research had a slower reduction in amplitude. When the frequency increased from 1.00 GHz to 1.18 GHz, there was a decrease of 13.0 W, while the comparison literature showed a decrease of 8.7 W to 8.5 W, thus proving the power stability of the improved structure in a wide frequency range. Besides nominal specifications, the robustness of the proposed circuit under practical non-ideal conditions was also evaluated. Full-wave method-of-moments solver in Advanced Design System was adopted for electromagnetic modeling, with conductor surface roughness and dielectric dispersion included in S-parameter simulations. Minor discrepancies between simulated and measured results mainly come from unmodeled solder mask edge effects and connector parasitic parameters. For fabrication tolerances, line width and gap deviations of ±0.02 mm led to a 1.8% variation in odd- and even-mode impedance, causing IL shifts of 0.1–0.2 dB and a 15 MHz center frequency offset, all within acceptable limits. Analysis on Rogers 4350B substrate showed that a ±2% permittivity fluctuation (3.48 ± 0.07) resulted in a 1.5% passband edge shift, and a ±5 μm thickness deviation changes characteristic impedance by less than 0.8 Ω, while RL remained above 14 dB. For SMP1340-007LF PIN diodes, a ±10% variation in reverse-biased junction capacitance (2.0 ± 0.2 pF) degraded off-state isolation by less than 1.2 dB. A ±15% change in forward-biased series resistance (0.13 ± 0.02 Ω) increased IL by no more than 0.08 dB. The results verify the design maintains favorable performance stability against fabrication and component variations.

5. Conclusion

This study aims to solve the impedance mismatch problem in discrete cascaded RFFE architectures while achieving single-chip integration of filtering, switching, and phase-shifting functions. To this end, the CML structure was improved, a PIN-diode bias network was introduced to regulate the operating modes, and the transmission zeros were analyzed via an odd-/even-mode cooperative model. A PCML and slow-wave resonator structure was designed, and a monolithic integration scheme for filter switches and PSs was constructed, optimizing impedance matching and frequency selectivity. The results showed that the IL of the filter switch at the center

frequency of 0.6 GHz was 1.3 dB, the turn off suppression was 30 dB, the relative bandwidth was 33.3%, and the IL was reduced by 43.4% and the isolation was improved by 18.6% compared to traditional discrete designs; The filtering PS had an IL of 0.65 dB at the center frequency of 3 GHz, a PSD of 0.9°, a power capacity of 27 W, a phase accuracy improvement of 64% compared to reference [29], and a power carrying capacity improvement of 100% compared to reference [31]. The improved coupling structure achieved better out-of-band suppression than 55 dB within the 2.5–4.1 GHz passband, with an RL below 15 dB, achieving efficient synergy between filtering switching and filtering phase shifting functions. This study proposes a monolithic integration scheme for filtering, switching, and phase shifting based on an improved CML structure. By introducing a PIN diode bias network and a slow-wave resonant cavity, the design effectively optimizes impedance matching and frequency selectivity. Experimental results demonstrate that the structure maintains good filtering performance while achieving low IL and high isolation. This integrated approach provides a feasible circuit implementation to address the issues of impedance mismatch and volume redundancy in traditional discrete architectures, contributing to the development of RF front-end modules with higher integration and improved performance. The current research on filtering circuits is limited to the mid to low frequency range, and the phase stability in high-temperature environments has not been verified. In the future, it can be extended to the millimeter wave frequency band, using aluminum nitride ceramic substrates to enhance power capacity and thermal stability. Machine learning algorithms can be introduced to optimize multi-objective parameter design, exploring tunable coupling structures based on novel two-dimensional materials to achieve broadband, intelligent RFFE system integration.

Reference

[1] SHOME, P. P., KHAN, T., KOUL, S. K., et al. Filtenna designs for radio-frequency front-end systems: A structural-oriented review. *IEEE Antennas and Propagation Magazine*, 2021, vol. 63, no. 5, p. 72–84. DOI: 10.1109/MAP.2020.2988518

[2] HSU, T., LUO, Z., GUPTA, A., et al. A low-cost and low-power solution for RF-front-end impedance tuning with high-voltage solid-state switches. *IEEE Microwave Magazine*, 2025, vol. 26, no. 6, p. 113–118. DOI: 10.1109/MMM.2024.3479989

[3] MA, L., WANG, L., CHEN, X. Design of 4x4 multi-layer Butler-like matrix with flexible phase differences and filtering integration for 5G applications. *Applied Computational Electromagnetics Society Journal*, 2025, vol. 40, no. 2, p. 130–137. DOI: 10.13052/2025.ACES.J.400206

[4] YANG, D., DONG, Y. Miniaturized integrated bandstop filter with high in-band performance based on substrate integrated coaxial line. *IEEE Electron Device Letters*, 2025, vol. 46, no. 6, p. 1003–1006. DOI: 10.1109/LED.2025.3558979

[5] SALMANI, R., BIJARI, A., ZAHIRI, S. H. A compact dual-band bandpass filter using coupled microstrip lines. *IETE Journal of Research*, 2023, vol. 69, no. 12, p. 8554–8560. DOI: 10.1080/03772063.2022.2074898

[6] QIN, P. Y., WEI, F., GUO, Y. J. A wideband-to-narrowband tunable antenna using a reconfigurable filter. *IEEE Transactions on Antennas and Propagations*, 2015, vol. 63, no. 5, p. 2282–2285. DOI: 10.1109/TAP.2015.2402295

[7] RAJIAN, P., TAVAKOLI, M. B., SETOUDEH, F., et al. Advanced design and analytical modeling of multiband bandpass filters using interconnected multimode resonators and multi-level impedance structures. *International Journal of Engineering*, 2025, vol. 38, no. 9, p. 2196–2207. DOI: 10.5829/ije.2025.38.09c.15

[8] KUMAR, A., RAMKUMAR, S., JHARIYA, D. K. A compact differential wideband bandpass filter with good out-of-band performance. *Electromagnetics*, 2025, vol. 45, no. 5, p. 359–370. DOI: 10.1080/02726343.2025.2472074

[9] MEYER, E., VERTEGAAL, C., JOHNSON, L., et al. Substrate integrated waveguide pedestal filtering-antenna and arrays for 5G radio frequency front-ends. *International Journal of Microwave and Wireless Technologies*, 2023, vol. 15, no. 8, p. 1283–1290. DOI: 10.1017/S175907872300034X

[10] YUN, S., CHO, C., JO, S., et al. A 2.7-dB NF 55-dBm IIP2 blocker-tolerant receiver front end employing dual RF and BB N-path filters for 5G new radio cellular applications. *IEEE Transactions on Microwave Theory and Techniques*, 2025, vol. 73, no. 3, p. 1558–1572. DOI: 10.1109/TMTT.2024.3457841

[11] WEI, F., DING, X. Z., LIU, X., et al. Balanced filtering phase shifters with low phase deviation and high common-mode suppression. *IEEE Transactions on Circuits and Systems I, Regular Papers*, 2023, vol. 70, no. 7, p. 2814–2822. DOI: 10.1109/TCSI.2023.3265085

[12] CHOI, H., SONG, M., LEE, J. Novel transmission-line circuit configuration of cross-coupled filter with negative coupling. *IEEE Transactions on Microwave Theory and Techniques*, 2024, vol. 72, no. 8, p. 4842–4853. DOI: 10.1109/TMTT.2024.3357932

[13] LEE, J., JIN, H., LEE, G., et al. A 28/37-GHz frequency-reconfigurable dual-band 1-channel front-end IC for 5G communication radios." *IEEE Transactions on Microwave Theory and Techniques*, 2025, vol. 73, no. 4, p. 1882–1895. DOI: 10.1109/TMTT.2024.3483454

[14] CAI, J., WANG, J., OU, M., et al. A high-power S-band waveguide phase shifter with rotary RF chokes. *IEEE Microwave and Wireless Technology Letters*, 2024, vol. 34, no. 4, p. 383–386. DOI: 10.1109/LMWT.2024.3349976

[15] LI, H., JIN, B., WU, Y., et al. A behavioral model for RF vector-sum phase shifter. *International Journal of Numerical Modelling: Electronic. Networks, Devices, and Fields*, 2024, vol. 37, no. 2, p. 1–9. DOI: 10.1002/jnm.3202

[16] ZAIDI, A. M., KANAUJIA, B. K., KISHOR, J., et al. Design techniques for passive planar reconfigurable RF circuits: Reconfigurable RF circuits. *IEEE Microwave Magazine*, 2024, vol. 25, no. 9, p. 29–42. DOI: 10.1109/MMM.2024.3412448

[17] REZAEI, A., YAHYA, S. I., NOURI, L. An ultra-compact diplexer based on simple microstrip coupled lines for GSM and wideband wireless applications. *Wireless Networks*, 2024, vol. 30, no. 2, p. 857–865. DOI: 10.1007/s11276-023-03519-x

[18] ERDIN, I., ACHAR, R. Indefinite impedance matrix techniques for power integrity analysis of multilayered printed circuits. *IEEE Transactions on Electromagnetic Compatibility*, 2023, vol. 65, no. 6, p. 1734–1743. DOI: 10.1109/TEMC.2023.3312773

[19] MUSHTAQ, B., KHALID, S. Design of miniaturized single and dual-band bandpass filters using diamond-shaped coupled line resonator for next-generation wireless systems - Erratum. *International Journal of Microwave and Wireless Technologies*, 2023, vol. 15, no. SI10, p. 1809–1809. DOI: 10.1017/S1759078723000399

[20] CHOWDHURY, A., RANJAN, P. A novel PIN diode-based frequency reconfigurable patch antenna with switching between the mid-5G and high-5G frequency band. *International Journal of Microwave and Wireless Technologies*, 2024, vol. 16, no. 4, p. 595–604. DOI: 10.1017/S1759078723001149

[21] SUMAN, P. N., MISHRA, G. K. Frequency and pattern reconfigurable arrow shape patch antenna with a PIN diode. *Frequenz*, 2025, vol. 79, no. 5–6, p. 287–292. DOI: 10.1515/freq-2024-0211

[22] YASIN, F. N. M., SHAIRI, N. A., OTHMAN, A., et al. High isolation of SPDT PIN diode switch using switchable dumbbell-shaped DGS in millimeter wave 28 GHz band. *Bulletin of Electrical Engineering and Informatics*, 2023, vol. 12, no. 6, p. 3509–3516. DOI: 10.11591/eei.v12i6.6071

[23] SARON, S., CHAUDHARY, G., JEONG, Y. Concurrent dual-band shifter with independent tunable phase shift control. *IEEE Microwave and Wireless Technology Letters*, 2024, vol. 34, no. 2, p. 163–166. DOI: 10.1109/LMWT.2023.3345950

[24] VERMA, R. P., SAHU, B., GUPTA, A. A miniaturized UWB bandpass filter with tunable cut-off frequencies employing rectangular open-loop defected ground structure. *International Journal of Microwave and Wireless Technologies*, 2023, vol. 15, no. 10, p. 1689–1697. DOI: 10.1017/S1759078723000594

[25] GUPTA, A., KHAN, A. A. Planar dual-band bandpass filter with regular harmonic suppression. *International Journal of Microwave and Wireless Technologies*, 2024, vol. 16, no. 8, p. 1397–1404. DOI: 10.1017/S1759078724000795

[26] WANG, Z., LI, X., SHEN, C., et al. A switched flexible dual-mode bandpass filter tuned by organic electrochemical transistor. *IEEE Microwave and Wireless Technology Letters*, 2025, vol. 35, no. 2, p. 197–200. DOI: 10.1109/LMWT.2024.3507753

[27] LI, H., XU, J., ZHANG, X. Compact on-chip mm-wave reconfigurable wideband filtering switch in 28-nm bulk CMOS for integrated sensing and communication system applications. *IEEE Transactions on Circuits and Systems I: Regular Papers*, 2025, vol. 72, no. 1, p. 125–134. DOI: 10.1109/TCSI.2024.3464734

[28] HUANG, X., JIA, H., DONG, S., et al. A 24–30 GHz four-element phased-array transceiver with low-insertion-loss compact T/R switch and bidirectional phase shifter for 5G communication. *IEEE Transactions on Very Large Scale Integration (VLSI) Systems*, 2023, vol. 31, no. 11, p. 1839–1851. DOI: 10.1109/TVLSI.2023.3308720

[29] WANG, Q., WEI, F., DING, X., et al. A wideband reconfigurable filtering phase shifter based on stub-loaded multimode resonators. *Frequenz*, 2025, vol. 79, no. 3–4, p. 167–173. DOI: 10.1515/freq-2024-0167

[30] TIAN, Y., ZHANG, Y., GU, J., et al. Design and analysis of a 26-32-GHz 6-bit passive vector modulation phase shifter for CMOS bidirectional transceiver. *IEEE Transactions on Very Large Scale Integration (VLSI) Systems*, 2025, vol. 33, no. 3, p. 673–684. DOI: 10.1109/TVLSI.2024.3490618

[31] SPAETH, M., NEUDER, R., SCHUESSLER, M., et al. Multigap-waveguide liquid crystal phase shifter at Ka-band. *IEEE Microwave and Wireless Technology Letters*, 2025, vol. 35, no. 3, p. 294–297. DOI: 10.1109/LMWT.2025.3527029

[32] FENG, L., CHEN, J., YU, X., et al. A novel wideband 90° filtering phase shifter using broadside-coupled MSLs. *IEEE Transactions on Circuits and Systems II: Express Briefs*, 2022, vol. 69, no. 6, p. 2742–2746. DOI: 10.1109/TCSII.2022.3145872

[33] CHEN, X., WEI, Z., CHI, P.-L., et al. Design and synthesis of reconfigurable filtering phase shifter using optimization of coupling matrix. *IEEE Transactions on Microwave Theory and Techniques*, 2022, vol. 70, no. 8, p. 3886–3896. DOI: 10.1109/TMTT.2022.3186376

About the Authors ...

Dan WANG (1983.02, Female, Meishan, Sichuan, Han) obtained a Master's degree from the University of Electronic Science and Technology of China (UESTC) in 2009, Major in Electromagnetic Field and Microwave Technology; obtained a Bachelor's degree from the Southwest University of Science and Technology (SWUST) in 2006, Major in Electronic Information Engineering. Research focus: Microwave circuits; 2009–2014: Designer, Chengdu Fire Control Technology Center. 2015–2016: Designer, Aumiwalker Technology Co., Ltd. 2016–2018: Designer, Chengdu Hongke New Materials Electronics Co., Ltd. 2018–present: Full-time lecturer, School of Network and Communication Engineering, Chengdu Technological University. Published 1 EI-indexed journal academic paper, led 2 university-level research projects.

Qiaochu XIE (corresponding author, 1991.10, Male, Zigong, Sichuan, Han) obtained a Master's degree from the School of Automation and Information Engineering, Sichuan University of Technology in 2017, Major in Control Science and Engineering; obtained a Bachelor's degree from Mechanical Engineering and Automation College of Xihua University in 2014, Major in Automation Engineering. Research Focus: Big data; 2018–present: Full-time experimenter, School of Network and Communication Engineering, Chengdu Technological University; led 3 university-level research projects.